International Journal of Technology

http://ijtech.eng.ui.ac.id

Research Article

Exploring pH-Controlled Hydrothermal SnO_2 Nanomaterials from Local Indonesian Precursor for Methylene Blue Dye Degradation

Nelson Jap[1], Akhmad Herman Yuwono[1,2,3*], Nofrijon Sofyan[1,2], Donanta Dhaneswara[1,2], Fairuz Septiningrum[1], Eka Nurhidayah[1], Fakhri Akbar Maulana[1], Danang Pamungkas Priambodo[3], Rizqi Ardi Habibie[1], Sudirman[4], Veinardi Suendo[4], Yahya Winda Ardianto[5], Ria Wardhani Pawan[5]

[1]Department of Metallurgical and Materials Engineering, Faculty of Engineering, Universitas Indonesia, Depok, 16424, Indonesia

[2]Advanced Materials Research Center (AMRC), Faculty of Engineering, Universitas Indonesia, Depok, 16424, Indonesia

[3]Energy Transition Laboratory, Interdisciplinary Engineering Research Unit-Faculty of Engineering, Universitas Indonesia, Depok 16424, Indonesia

[4]Division of Inorganic and Physical Chemistry, Faculty of Mathematics and Natural Sciences, Institut Teknologi Bandung, Bandung 40132, Indonesia

[5]PT. Timah Industri, Cilegon, Banten 42436, Indonesia

[*]Corresponding author: ahyuwono@eng.ui.ac.id, Tel.: +6281314099878

Abstract: Tin oxide (SnO_2) as a wide bandgap semiconductor shows promising photocatalytic properties; however, commercially available precursors, which are costly, are often used to develop its nanomaterial. With its abundant natural resources, Indonesia has the potential to replace these commercial precursors with locally sourced alternatives. This study explores the synthesis of SnO_2 using a local tin chloride ($SnCl_4$) and investigates its photocatalytic performance through methylene blue degradation. The SnO_2 samples were synthesized using the hydrothermal process at 180 °C for 24 h. Furthermore, to optimize the process, the pH of the solution was also tuned at 1, 7, and 11 to analyze its effect on material properties. Characterization techniques, including X-ray diffraction, scanning electron microscopy, energy-dispersive X-ray spectroscopy, UV-Vis spectroscopy, particle size analyzer, zeta potential, and N_2 adsorption-desorption analysis, were used to evaluate the structural, morphological, and optical properties of the synthesized materials. The samples synthesized in all pH conditions after the hydrothermal process were confirmed to be tetragonal rutile SnO_2. Additionally, the crystallite size, optical properties, and morphology of the samples are affected by different pH conditions. SnO_2 synthesized at pH 11 has a high BET surface area of 132.12 m^2/g and mesoporous properties. The photocatalytic performance of the synthesized SnO_2 achieved a degradation of methylene blue over 95% using UV irradiation for 120 min. The high degradation of dye can be attributed to the adsorption capability exhibited by the high surface area of the synthesized sample. This study proves that SnO_2 synthesized using locally sourced $SnCl_4$ shows comparable photocatalytic performance to commercial materials.

Keywords: Adsorption; Hydrothermal; pH control; Photocatalyst; SnO_2

1. Introduction

The decline of the world's water source quality caused by water pollution threatens human health. Approximately 70 billion tons of water flow are polluted every year by synthetic dyes that contain harmful industrially produced compounds in the form of aromatics and heavy metals (Dutta et al., 2024; Lin et al., 2023). Recently, the advanced oxidation process (AOP) has

https://doi.org/10.14716/ijtech.v17i2.8207
Received July 2025; Revised November 2025; December 2025

attracted considerable attention due to its strong oxidation capability and ability to remediate dangerous dyes into less harmful and safer byproducts (Khan et al., 2024). AOPs can be used using photocatalysts that are non-selective, have high efficiency, and react with light, making them viable for degrading organic pollutants (Khader et al., 2024).

Research on inorganic semiconductor photocatalysts has mostly used metal oxides, such as WO_3, TiO_2, ZnO, CeO_2, and SnO_2 (Mohamadpour and Amani, 2024). Among these materials, tin oxide (SnO_2) is a promising candidate as a photocatalyst because of its high stability, non-toxicity, high oxidation potential, economic feasibility, and environmental safety (Sun et al., 2022). SnO_2 is an n-type semiconductor with a rutile crystal structure and a bandgap value of 3.6 eV, indicating high optical transparency in visible light and high photoactivation capabilities in UV light (Das and Jayaraman, 2014). Previous studies have proven that SnO_2 reached about 80–90% of methylene blue degradation irradiated under UV light, indicating it as a potential photocatalytic material (Luque et al., 2020; Honarmand et al., 2019; Kim et al., 2016).

The synthesis of SnO_2 photocatalysts utilizes various methods, such as sol-gel, co-precipitation, hydrothermal, electrochemical, microwave-assisted, and solution combustion synthesis (Shabna et al., 2023). The hydrothermal process is a promising method because of its simplicity and scalability, yielding nanomaterials with favorable properties (Yu et al., 2023; Byrappa and Adschiri, 2007). The synthesis of hydrothermal SnO_2 commonly uses Sn hydrated salts, such as $SnCl_2{\cdot}2H_2O$ (Li et al., 2009) and $SnCl_4{\cdot}5H_2O$ (Talebian and Jafarinezhad, 2013). The pH conditions could also be modified to optimize the process, offering a simple method to optimize the process by influencing the structural, optical, and morphological properties of SnO_2 (Sukriti and Chand, 2019).

Indonesia, which is known for its abundance of tin (Sn) across the Bangka Islands, shows major potential for providing Sn chemical precursors for SnO_2 nanomaterial synthesis. Indonesia has a total amount of cassiterite mineral of 2.76 tons (Schwartz et al., 1995). Extensive exploration is needed in using locally sourced minerals as chemical precursors for the research and development of SnO_2 photocatalysts. Prior to this research, the local anhydrous $SnCl_4$ was utilized for fabricating conductive glass (Lalasari et al., 2018) and electron transport layers (Yuwono et al., 2023); however, no attempts have been made to use this local precursor for the synthesis of SnO_2 as a photocatalyst. Hence, this study aims to explore the properties of hydrothermally synthesized SnO_2 under various pH conditions using local anhydrous $SnCl_4$. Additionally, pH was modified at 1, 7, and 11 to simulate acidic, neutral, and basic conditions using NH_3 as an alternative weaker base, compared to previous studies that used strong bases (NaOH or KOH) (Zhang et al., 2025; Sato et al., 2013). The resulting materials were then tested for methylene blue degradation using UV irradiation to further observe their photocatalytic activity and adsorbent properties.

2. Materials and Methods

2.1 Materials

The synthesis of hydrothermal SnO_2 were prepared with local anhydrous $SnCl_4$ (99%, PT Timah Industri, Cilegon, IDN), NaOH pellets (Merck, Darmstadt, DE), NH_3 (25%, Merck, Darmstadt, DE), and HCl (37%, Merck, Darmstadt, DE). SnO_2 nanopowder (Sigma-Aldrich, St. Louis, USA) will also be used as the main standard (Code: STD) for comparison of performance. Distilled water was used as the solvent to prepare all the solutions within the experiment.

2.2 Methods

The preparation of the solvent for SnO_2 starts with the dilution of the initial $SnCl_4$ anhydrous to a final concentration of 0.08 M. As much as 40 ml of the precursor solution was taken and then mixed with 10 ml of 10 mmol NaOH solution that was prepared beforehand. The solution was then stirred at 700 rpm for 30 min. The initial solution without any modifications had a pH of 1 (sample **TO-1**). Notably, the addition of NaOH causes no change in the solution

pH, as it remains at 1. Subsequently, NH_3, as the pH modifier, was added dropwise before the hydrothermal process until the final pH reached 7 (sample **TO-7**) and 11 (sample **TO-11**). When the solution reached pH 7, white precipitates were formed, turning the clear solution into a white liquid. At pH 11, the white precipitates dissolved back into the solution, forming a clear but blurry solution.

After the stirring process was completed, the prepared solution (50 ml in total volume) was transferred to an 80 ml Teflon chamber and tightly sealed inside a stainless steel autoclave. The hydrothermal process was conducted using an autoclave inside an electric oven pre-heated at 180 °C. After 24 h, the autoclave was left to cool until it reached room temperature. The resulting product was divided into its supernatant and precipitate. The precipitate was washed with distilled water until it reached a neutral pH level. After washing, the resulting precipitate was dried for 24 hours at 100 °C inside an oven and was then crushed using an agate mortar and pestle for characterization and photocatalytic performance tests.

2.3 Materials Characterization

The phase and structural characteristics of the samples were measured using a PANalytical Empyrean (Malvern PANalytical, Almelo, Netherlands) X-ray diffractometer (XRD) with a CuKα radiation source ($\lambda = 1.5406$ Å). Samples were scanned from 2θ of 10–90° with scan rate of 0.195°/s and step size of 0.026°. Structural parameters, such as crystallite sizes, were calculated using Scherrer's equation (Equation 1) (Suryanarayana and Norton, 1998) and Williamson-Hall relation (Equation 2), where the lattice strain (ε) relation is denoted in Equation 3 (Pandey et al., 2015):

$$d = \frac{K\lambda}{\beta \cos\theta} \tag{1}$$

$$\beta \cos\theta = \frac{K\lambda}{d} + 4\varepsilon \sin\theta \tag{2}$$

$$\varepsilon = \frac{\beta}{4 \tan\theta} \tag{3}$$

where d (nm), the crystallite size, is inverse to β which represents the full width at half maximum (FWHM) of peaks and the Bragg angle (θ). The values proportional to d are the shape factor, K (0.94) and the X-ray wavelength, λ.

The morphological characteristics and elemental composition of the samples were inspected using field emission–scanning electron microscopy (FE-SEM) and energy-dispersive X-ray spectroscopy (EDS) using the FEI Quanta 650 FEG (FEI, Oregon, USA). The optical properties of the SnO_2 are observed using a UV-Vis diffuse reflectance spectroscopy (DRS) in a ThermoScientific Evolution 220 (Thermo Fisher Scientific, Massachusetts, USA) with $BaSO_4$ as a reference. The corresponding absorption spectra were obtained from the transformed reflectance data through the Kubelka-Munk function ($F(R_\infty)$) based on Equation 4 (Makuła et al., 2018):

$$F(R_\infty) = \frac{K}{S} = \frac{(1-R)^2}{2R} \tag{4}$$

where K and S are the absorption and scattering coefficients, respectively. Both coefficients can be calculated based on the sample's reflectance (R).

The bandgap energy from the synthesized samples were quantified using Tauc's relation (Equation 5) (Klein et al., 2023; Makuła et al., 2018):

$$(\alpha h\nu)^{\frac{1}{n}} = A(h\nu - E_g) \tag{5}$$

where $h\nu$ is the total energy in relation to the photon absorption coefficient, α, which is proportional to $F(R_\infty)$. A is the constant and E_g denotes the band gap energy according to

the band structure characteristics represented by the n value in the equation. The exponential value n of 2 indicates an indirect transition, while $\frac{1}{2}$ describes a direct transition.

For further characterization of the photocatalytic properties, particle size analysis (PSA) and zeta potential analysis of diluted samples were performed using the Otsuka ELSZneo (Otsuka, Osaka, Japan). For sample preparation, 10 mg of the obtained particles were weighed and diluted in 10 ml of distilled water. Subsequently, the suspension was sonicated for 10 min until the solution was transparent. Testing was conducted directly after sonication with a flat surface cell and repeated 3 times to determine the average particle size and zeta potential.

N_2 adsorption-desorption characteristics followed with Brunauer-Emmett-Teller (BET) specific surface area and Barrett-Joyner-Halenda (BJH) desorption pore size distributions with Micromeritics 3Flex (Micromeritics, Georgia, USA). Degassing conditions were conducted at 120 °C for 2 h and measured at a full isotherm condition on a partial pressure range of 0.05–0.998.

2.4 Investigation of Adsorption–Photocatalytic Performance

The photocatalytic activity of the samples was tested using 10 ppm methylene blue dye (MB) with a custom-made photoreactor using UV light mounted with 3 mercury vapor lamps (125 Watts each, 220–240 Volts). The procedure was tested using 100 ml of dye solution mixed with 50 mg of the photocatalyst. The test was conducted for 30 min in the dark condition at time increments of 5, 10, 15, 20, and 30. During irradiation, the sample-to-lamp distance was set at approximately 20 cm, with 3700 lumens/m^2 and tested at room temperature. The total testing time was 120 min with increments of 5, 10, 15, 20, 30, 45, 60, 90, and 120 min. An aliquot of 5 ml was taken from the mix and centrifuged to separate the photocatalyst and the supernatant between each time increment. The initial concentration of MB and changes in the supernatant were measured with a UV-Vis spectrophotometer at 665 nm. The resulting data were then used to calculate the dye degradation percentage (Equation 6) (Septiningrum et al., 2024):

$$\text{Degradation}\% = \left(\frac{A_0 - A}{A_0}\right) \times 100\% \tag{6}$$

The A_0 denotes the initial absorbance of MB before degradation, and A signifies the changes in absorbance after degradation performance testing. Based on the changes in absorbance, kinetic analysis was also conducted based on the first-order reaction denoted in (Equation 7) (Sagadevan et al., 2022):

$$\ln\left(\frac{A_0}{A}\right) = kt \tag{7}$$

where k describes the rate constant value with respect to the changes in time (t). The value of k is represented by the slope of the linearly fitted degradation results based on the changes of A after testing.

3. Results and Discussion

3.1 Crystal Structure of the Hydrothermal SnO_2

The XRD pattern of the as-synthesized samples at all pH values are shown in Figure 1. Structural analysis showed that the diffraction pattern corresponded to tetragonal rutile SnO_2 (ICDD 01-077-0448), and no other phases were observed. The rutile phase conforms to the 2θ of 26.6°, 33.9°, 37.9°, 51.8°, 54.7°, 57.8°, 61.9°, 65.9°, 71.3°, 78.7°, 83.7° from the database, with each value corresponding to the (110), (101), (200), (211), (220), (002), (310), (301), (202), (321), and (222) planes. Despite the differing pH conditions during the hydrothermal process, no distinct difference in peak positions was observed. However, in terms of their intensity, the peaks in TO-7 and TO-11 are different from those in TO-1, evident from the broadening of peaks at (110) and (101), indicating that the crystals experience strain.

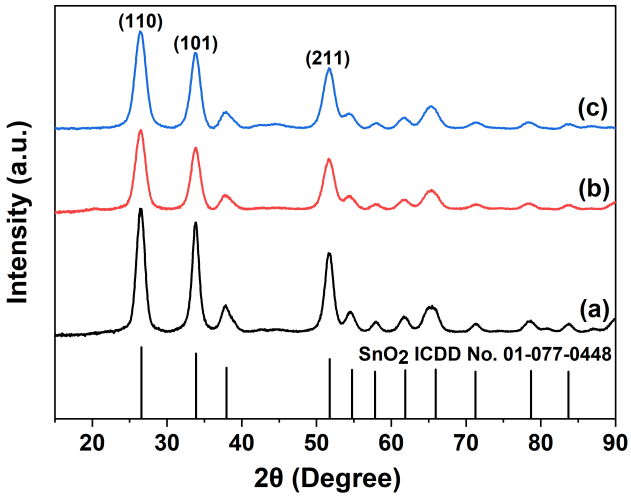

Figure 1 XRD patterns of synthesized samples: (a) TO-1, (b) TO-7, and (c) TO-11

Table 1 presents the crystallite sizes and crystallographic parameters from all the samples. The lattice parameters of SnO_2 from all the samples show values similar to those in the database (ICDD 01-077-0448), further confirming that they have a tetragonal crystal structure. Based on Scherrer's equation and Williamson-Hall relation, the pH increase from TO-1 to TO-11 causes the crystallite size to decrease. The lattice parameters also shifted when the synthesis were at neutral and basic conditions, which might be attributed to strain within the crystal. The results of calculation ε signify that SnO_2 crystals experience more strain as the synthesis pH increases. Furthermore, the negative strain value indicates that the crystal structure experiences compressive strain (Kerrami et al., 2020). The decrease in the crystallite size and strain in crystals can be correlated with the formation mechanism of crystals during the hydrothermal process. The reaction proposed in the formation of SnO_2 with the hydrothermal process is written as (Reaction 1) (Wan et al., 2018):

$$Sn(OH)_6^{2-} \rightarrow SnO_2 \downarrow + 2OH^- + 2H_2O \quad (1)$$

Table 1 Crystallographic calculations for all synthesized samples

Sample code	Scherrer Crystallite Size (nm)	Williamson-Hall Crystallite Size (nm)	Microstrain $\varepsilon \times 10^{-3}$	Lattice Parameter		
				a = b (Å)	c (Å)	Unit Cell Vol.
ICDD 01-077-0448	-	-	-	4.739	3.187	71.570
TO-1	7.04	5.09	-3.8	4.753	3.183	71.927
TO-7	5.86	4.23	-4.5	4.760	3.180	72.046
TO-11	5.51	3.69	-6.2	4.760	3.180	72.058

Under high temperature and pressure conditions, the Sn species inside the solution hydrolyze into an ionic complex with a Sn^{4+} oxidation state. The ionic complex will then dissolve within the solution, and after reaching its supersaturated state, it will precipitate and decompose into SnO_2 (Jensen et al., 2012; Mamakhel et al., 2020). Different ratios of H^+ and OH^- ions affect the solubility rate during the hydrothermal process. A larger solubility rate is obtained when the OH^- species present is more dominant in the solution, promoting individual crystallization at a faster rate (Zhang et al., 2025). The larger crystallite size from TO-1 can be further correlated with the formation mechanism of the SnO_2 during the hydrothermal process. Under

neutral and basic conditions, the concentration of OH^- ions is relatively higher than that under acidic conditions, causing the formation of complexing ions to be faster and individual nuclei to likely appear during the process. With a low concentration of OH^- ions in the acidic condition, formation of the $Sn(OH)_6^{2-}$ becomes slower, causing crystal aggregation during the growth process (Wu et al., 2002). Based on the described interactions and results, pH modification affects the structural properties of the SnO_2 crystal.

3.2 Morphology of the Hydrothermal SnO_2

Morphological characteristics from as-synthesized samples are shown in Figure 2. The particles have irregular shapes with random sizes. The EDS results (see Table 2) also show that the synthesized samples can be confirmed as a compound of Sn and O with no impurities present.

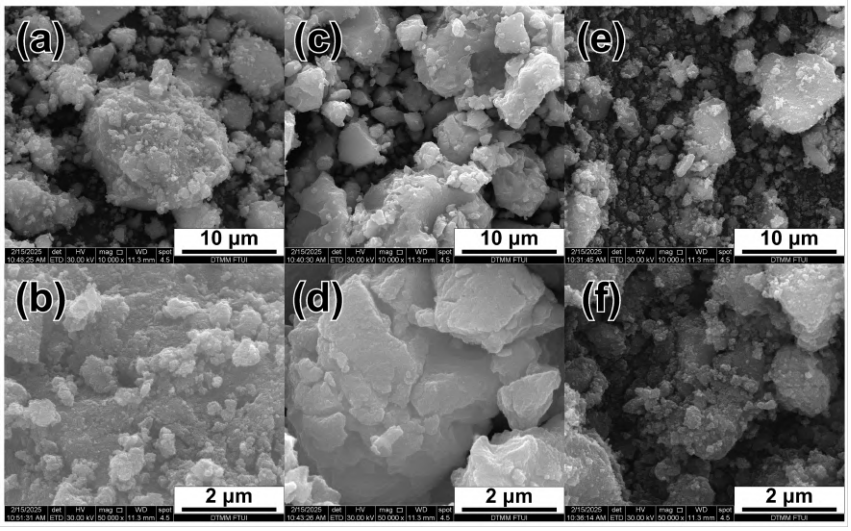

Figure 2 Morphology of the as-synthesized samples: (a-b) TO-1, (c-d) TO-7, and (e-f) TO-11

On closer inspection with a higher magnification, the large structures from TO-1 and TO-11 are formed by particles that are smaller than their large counterparts, as shown in Figure 2. The formation of bulk fragments consisting of smaller particles indicates agglomeration within the material (Sukriti and Chand, 2019). In contrast, the surface of particle TO-7 showed no smaller particles, indicating that agglomeration is not as severe.

Table 2 Mean particle size from PSA and elemental composition from EDS

Sample Code	Mean Particle Size (nm)	Elemental Composition (at%)			
		Sn	O	Na	Cl
TO-1	2121.0	18.39	81.61	–	–
TO-7	1975.9	31.44	68.56	–	–
TO-11	904.1	24.50	75.50	–	–

As the pH increases from the acidic condition, the bulk particles become smaller in size. This is further supported by the mean particle size results shown in Table 2, where the largest particle size is TO-1, followed by TO-7, which has a slightly smaller particle size, and the lowest particle size is TO-11. It is worth noting that although the PSA results show large mean sizes, smaller particles are visible based on the SEM results. This particle size discrepancy was probably caused by severe agglomeration from the small particles even after sample preparation, resulting in inaccurate and larger results. Nevertheless, it is still evident that the PSA results are related to SEM, where the particle size decreases as pH increases.

The interaction between the particle size and solution pH during the hydrothermal process is correlated with the forces involved during the growth process. Under acidic and basic conditions, the respective H+ or OH- ions have higher concentrations, resulting in larger ionic charge forces than Van der Waals forces, promoting individual particle nucleation and growth because of repelling forces from the same ionic charge. The Van der Waals forces are higher in a neutral condition, resulting in larger nuclei that can then grow into larger particles (Zhang et al., 2025). These differing interactions of charge forces during the growth of SnO_2 in the hydrothermal process influenced the nanoparticle morphology and size.

3.3 Optimal Properties of the Hydrothermal SnO_2

Optical characteristics of the obtained samples are presented through the transformed Kubelka-Munk spectra shown in Figure 3. The proportional absorption peaks from all samples were measured at wavelength value of 280-286 nm. At 300-375 nm, an absorption edge is observed and its characteristic can be confirmed as SnO_2 (Li et al., 2009; Mishra and Ahmaruzzaman, 2022). The effect of pH increase has no obvious effect on the absorption spectra of the SnO_2 synthesized.

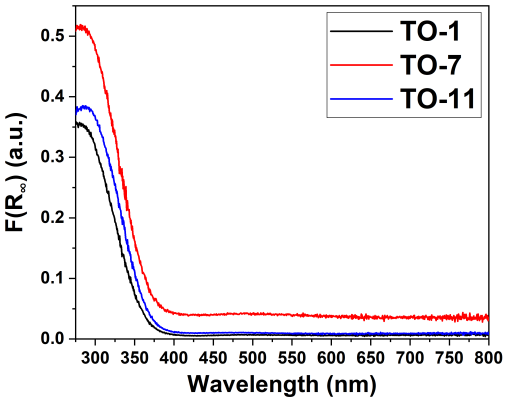

Figure 3 UV-Vis transformed Kubelka-Munk spectra of the corresponding SnO_2 samples

Based on the Tauc's relation, there is a difference in the E_g value from the materials at different pH conditions (see Table 3). SnO_2 itself has an E_g value of 3.60 eV, yet it is not clear whether the transition is indirect or direct—as previous studies have shown the possibility of exhibiting both natures (Karmaoui et al., 2018; Van Pham et al., 2021). Our calculations showed that the E_g value from the synthesized samples corresponded to SnO_2 when their structure was considered as a direct band gap (Table 2). Samples TO-1, TO-7, and TO-11 have direct E_g values of 3.639, 3.578, and 3.586 eV, respectively. It is worth mentioning that these values need further verification with computational methods.

Table 3 Bandgap energy of the synthesized SnO_2 samples.

Sample code	E_g (eV)	
	Indirect	Direct
TO-1	3.18	3.639
TO-7	3.13	3.578
TO-11	3.17	3.586

Previous studies have reported that increasing pH values also increases E_g, due to the decrease in crystallite sizes (Habte et al., 2020; Sukriti and Chand, 2019). In this study, the E_g decreased as the synthesis pH increased (Table 3). In the case of TO-1, the value of 3.639

eV corresponds closely to the bulk value of SnO_2, whereas TO-7 and TO-11 have E_g that is different from the initial TO-1. However, it can be observed that TO-7 and TO-11 have close E_g values, which can be correlated with the small difference in their crystallite sizes and similar unit cell volumes, as shown in Table 1.

3.4 Adsorption-Photocatalytic Study of Hydrothermal SnO_2

Photodegradation experiments on MB degradation were conducted according to the procedure described in the Methods section. The photodegradation performance of the synthesized samples were compared with the SnO_2 nanopowder as the standard (STD) (see Table 4). Figure 4 represents the change in MB concentration in each time increment during dark and irradiated conditions along with the photodegradation results indicated by the change in dye color. It was observed that the final degradation percentage from all samples reaches 90%, indicating that it can compete with STD.

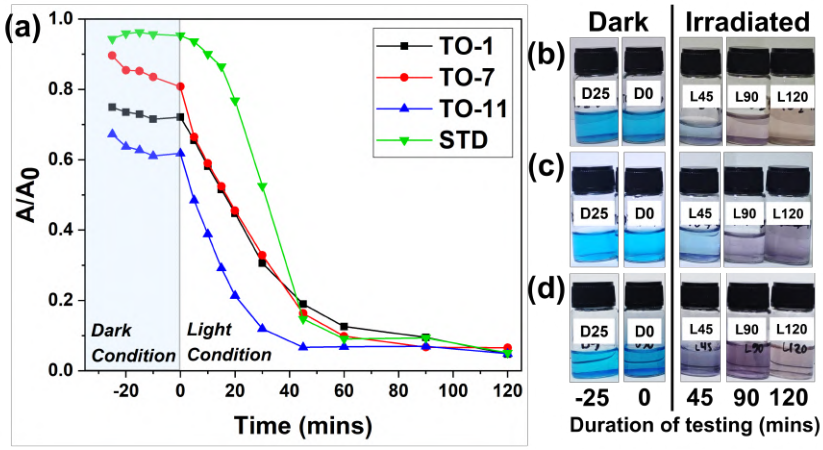

Figure 4 (a) Photodegradation performance results from the samples based on measured concentration changes. Changes in MB color during the adsorption-photocatalytic process are presented in bottles, with each row corresponding to samples (b) TO-1, (c) TO-7, and (d) TO-11

Table 4 Degradation percentage from tested samples in the dark (30 min) and irradiated conditions (120 min)

Sample code	Rate constant k (min^{-1})		Degradation (%)	
	Dark	Light	Dark - Minute 30	Light - Minute 120
STD	-2.19×10^{-4}	2.82×10^{-2}	4.53	91.72
TO-1	1.57×10^{-3}	2.29×10^{-2}	27.89	95.23
TO-7	3.78×10^{-3}	2.28×10^{-2}	19.22	93.44
TO-11	3.17×10^{-3}	1.91×10^{-2}	38.19	95.15

During tests in the dark, degradation of the synthesized samples was observed, signifying that an adsorption process occurred between the dye solution and the photocatalyst. The N_2 adsorption-desorption graph (see Figure 5) from the SnO_2 synthesized and STD showed a type IV isotherm. According to the IUPAC nomenclature, the hysteresis type corresponds to the H1 hysteresis, indicating that the synthesized samples are mesoporous (Thommes et al., 2015). Similar N_2 adsorption-desorption curves from SnO_2 have also been reported (Zhu et al., 2007; Fujihara et al., 2004). Samples TO-1, TO-7, and TO-11 exhibited high surface area, reaching 146.71, 143.88, and 132.12 m^2/g, respectively, which is significantly higher than STD, amounting to only 11.085 m^2/g.

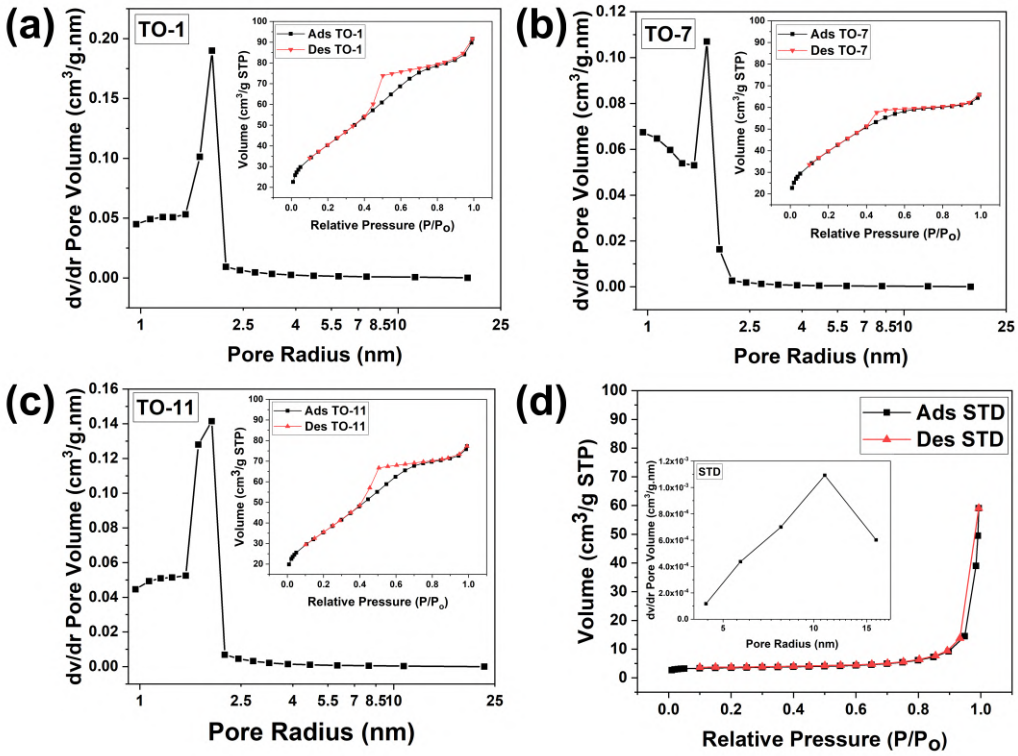

Figure 5 N_2 adsorption-desorption characteristics and pore size distribution from (a) TO-1, (b) TO-7, (c) TO-11, and (d) STD

Consequently, the high surface area can also be inversely correlated with the small pore size of materials (du Plessis, 2007). The BJH pore size distribution from the synthesized samples along with STD is presented in Figure 5. The pore sizes of samples TO-1, TO-7, and TO-11 were 1.93, 1.56, and 1.77 nm, respectively. In contrast, the STD sample had a large pore radius of 15.04 nm. The high surface area of the material and small pore size can enhance its adsorption capability, thereby increasing the degradation rate and final percentage of the MB (Gupta et al., 2022).

To verify the impact of surface area and pore size on adsorption kinetics, the first-order reaction rate is expressed in Figure 6a with the corresponding k value listed in Table 4. The highest adsorption rates were from TO-7, followed by TO-11 and TO-1, with STD being the lowest due to the low specific surface area and large pore size. Adsorption performance and kinetics are affected by the interplay of several factors, that include surface area, pore size, and volume distribution (Bavnhøj et al., 2019). Although TO-7 exhibited the highest rate constant, the sample still showed lower adsorption performance, which might be due to its lower surface area and pore volume values (see Figure 4) in the distribution compared to TO-1 and TO-11.

Interestingly, the highest adsorption performance was observed for TO-11 with a rate constant of $3.17 \times 10^{-3}\,\text{min}^{-1}$ and degradation percentage of 38.19% after 30 min of degradation testing in the dark. In contrast, samples TO-1 and TO-7 did not exhibit the same significant adsorption degradation percentage (see Table 4). Subsequently, degradation by the adsorption mechanism was not evident from the standard commercial SnO_2, only reaching 4.53% after testing in the dark for 30 min.

Additional characterizations were conducted to further study the adsorption properties of TO-11 and STD for comparison. The zeta potentials of samples TO-11 and STD were −21.92 and −31.05 mV, respectively. As a synthetic dye, MB has a cationic charge on its surface (Ighalo et al., 2021). With a negative zeta potential from the samples, differing charges causes an attraction from electrostatic forces, enhancing the adsorption capability of the photocatalysts (Azeez et al., 2018).

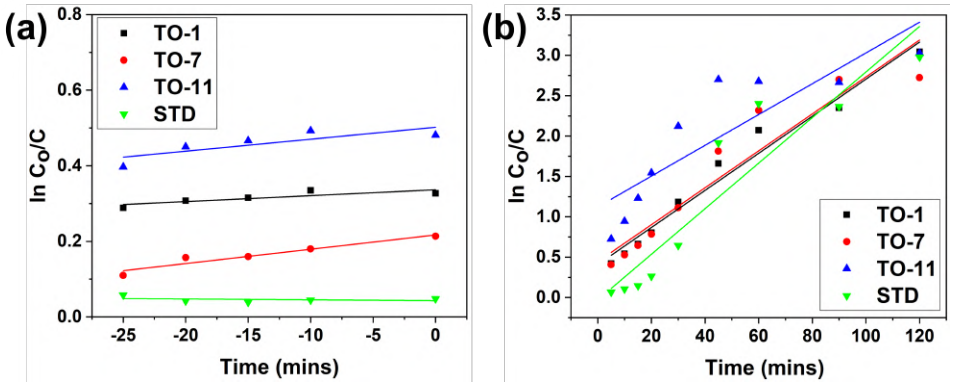

Figure 6 Kinetic analysis of the synthesized samples under (a) dark adsorption and (b) irradiated conditions

The degradation efficiency is then further boosted under light conditions, indicating that the degradation process involves a synergy between adsorption and photocatalytic activity (Jorgetto et al., 2023). This is further verified from the higher rate constant in irradiated conditions compared to dark conditions, with TO-1 being the highest, followed by TO-7 and TO-11 (Table 4). When compared to STD, degradation performance significantly rises in irradiated conditions, further closing the gap with synthesized samples in terms of performance at the 45-minute mark (Figure 4a). Consequently, the rate constant from STD is substantially greater for all the synthesized samples, marking its incomparable efficiency in terms of photocatalytic performance. Nonetheless, with the integration of adsorption and photocatalysis, the final degradation results of the synthesized samples were comparable with those of STD.

Based on the concentration changes under irradiated conditions, the proposed mechanism of photocatalysis from SnO_2 is based on the reaction described below (Skripkin et al., 2024; Sun et al., 2022) and further described in Figure 7:

$$SnO_2 + h\nu \rightarrow SnO_2\left(e^-_{(CB)}\right) + \left(h^+_{(VB)}\right) \tag{2}$$

$$SnO_2\left(h^+_{(VB)}\right) + H_2O \rightarrow SnO_2 + H^+ + OH^- \tag{3}$$

$$SnO_2\left(e^-_{(CB)}\right) + O_2 \rightarrow SnO_2 + O_2^- \tag{4}$$

$$\text{Methylene Blue} + OH^- \rightarrow CO_2 + H_2O \tag{5}$$

Based on the reactions mentioned, the photocatalysis mechanism can be divided into several stages. The first stage begins with photoexcitation, as described in Reaction (2), where an SnO_2 exposed to photons generates electron-hole pairs. Electrons are negatively charged particles from the valence band, while holes are positively charged and originate from the conduction band. The energy required for this reaction must meet or exceed the E_g of the semiconductor. Subsequently, photocatalysis continues with the formation of hydroxyl and superoxide radicals according to Reaction (3) and Reaction (4), respectively. As indicated in Reaction (5), hydroxyl radicals serve as oxidation agents for organic species that adsorb to the catalyst's surface and oxidize the dyes into intermediate compounds. Meanwhile, superoxide radicals contribute to the production of more radicals after protonation, which then leads to the formation of hydrogen peroxide (H_2O_2). The presence of H_2O_2 triggers subsequent derivative reactions, which produce radical species that aid the final oxidation of organic pollutants. The end products of dye degradation produces derivative compounds that are environmentally benign.

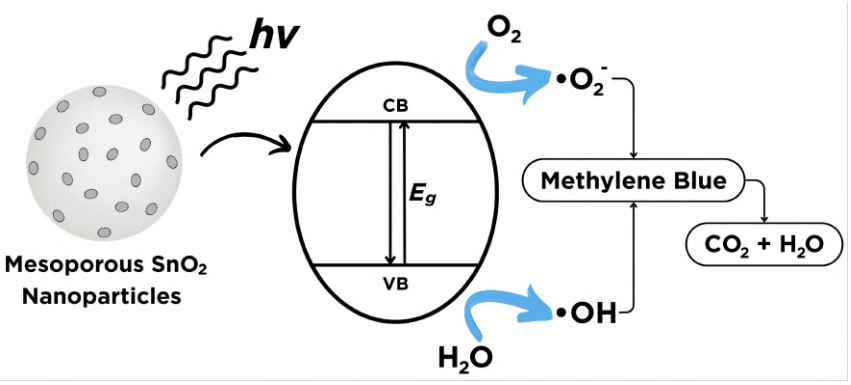

Figure 7 Proposed illustration on the adsorption-photocatalytic dye degradation mechanism

4. Conclusions

In conclusion, SnO_2 nanomaterials were successfully synthesized from locally sourced precursors via hydrothermal processing, with pH modification using NH_3 prior to synthesis enhancing their properties. Shifting from acidic to basic conditions produced the smallest crystallite and particle sizes, yielding mesoporous materials with an average BET surface area of 140 m^2/g. These property variations led to differing performances in methylene blue degradation, where the synthesized SnO_2 achieved up to 95% degradation, which is likely related to an adsorption-photocatalytic mechanism. Notably, sample TO-11 exhibited the highest degradation rate due to its large surface area and negative zeta potential. Despite some deviations from previous studies, such as reduced surface area and bandgap with increasing pH, the locally derived SnO_2 demonstrated performance comparable to standard materials. In addition, future investigations should be conducted to investigate on the optimization of synthesis procedures using locally sourced SnO_2 as photocatalysts.

Acknowledgements

The author expressed gratitude to Faculty of Engineering Universitas Indonesia for the funds provided for the research through the FTUI Professor Seed Grant Year 2023 with contract number of NKB-2616/UN2.F4.D/PPM.00.00/2023. The author would also like to extend their gratitude towards the team at Energy Transition Laboratory (ETL) at Interdisciplinary Engineering (IDE), Universitas Indonesia for characterization facilities used in this research.

Author Contributions

Nelson Jap: Conceptualization, Methodology, Investigation, Writing—original draft preparation; **Akhmad Herman Yuwono**: Conceptualization, Writing—review and editing, Supervision, Project administration, Funding acquisition; **Nofrijon Sofyan**: Resources, Supervision, Data curation; **Donanta Dhaneswara**: Resources, Supervision; **Fairuz Septiningrum**: Resources, Methodology; **Eka Nurhidayah**: Resources, Investigation; **Fakhri Akbar Maulana**: Resources, Visualization, Data Curation; **Danang Pamungkas Priambodo**: Investigation; **Rizqi Ardi Habibie**: Methodology; **Sudirman**: Data Curation, Investigation; **Veinardi Suendo**: Resources, Investigation; **Yahya Winda Ardianto**: Resources; **Ria Wardhani Pawan**: Resources.

Conflict of Interest

The authors declare no known conflicts of interest that might influence the outcome of the work reported in this article.

References

Azeez, F., Al-Hetlani, E., Arafa, M., Abdelmonem, Y., Nazeer, A., Amin, M., & Madkour, M. (2018). The effect of surface charge on photocatalytic degradation of methylene blue dye using chargeable titania nanoparticles. *Scientific Reports*, *8*(1). https://doi.org/10.1038/s41598-018-25673-5

Bavnhøj, C., Knopp, M., Madsen, C., & Löbmann, K. (2019). The role interplay between mesoporous silica pore volume and surface area and their effect on drug loading capacity. *International Journal of Pharmaceutics: X*, *1*, 100008. https://doi.org/10.1016/j.ijpx.2019.100008

Byrappa, K., & Adschiri, T. (2007). Hydrothermal technology for nanotechnology. *Progress in Crystal Growth and Characterization of Materials*, *53*(2), 117–166. https://doi.org/10.1016/j.pcrysgrow.2007.04.001

Das, S., & Jayaraman, V. (2014). Sno2: A comprehensive review on structures and gas sensors. *Progress in Materials Science*, *66*, 112–255. https://doi.org/10.1016/j.pmatsci.2014.06.003

du Plessis, M. (2007). Relationship between specific surface area and pore dimension of high porosity nanoporous silicon – model and experiment. *physica status solidi (a)*, *204*(7), 2319–2328. https://doi.org/10.1002/pssa.200622237

Dutta, S., Adhikary, S., Bhattacharya, S., Roy, D., Chatterjee, S., Chakraborty, A., Banerjee, D., Ganguly, A., Nanda, S., & Rajak, P. (2024). Contamination of textile dyes in aquatic environment: Adverse impacts on aquatic ecosystem and human health, and its management using bioremediation. *Journal of Environmental Management*, *353*, 120103. https://doi.org/10.1016/j.jenvman.2024.120103

Fujihara, S., Maeda, T., Ohgi, H., Hosono, E., Imai, H., & Kim, S.-H. (2004). Hydrothermal routes to prepare nanocrystalline mesoporous sno2 having high thermal stability. *Langmuir*, *20*(15), 6476–6481. https://doi.org/10.1021/la0493060

Gupta, A., Likozar, B., Jana, R., Chanu, W., & Singh, M. (2022). A review of hydrogen production processes by photocatalytic water splitting – from atomistic catalysis design to optimal reactor engineering. *International Journal of Hydrogen Energy*, *47*(78), 33282–33307. https://doi.org/10.1016/j.ijhydene.2022.07.210

Habte, A., Hone, F., & Dejene, F. (2020). Effect of solution ph on structural, optical and morphological properties of sno2 nanoparticles. *Physica B: Condensed Matter*, *580*, 411832. https://doi.org/10.1016/j.physb.2019.411832

Honarmand, M., Golmohammadi, M., & Naeimi, A. (2019). Biosynthesis of tin oxide (sno2) nanoparticles using jujube fruit for photocatalytic degradation of organic dyes. *Advanced Powder Technology*, *30*(8), 1551–1557. https://doi.org/10.1016/j.apt.2019.04.033

Ighalo, J., Iwuozor, K., Igwegbe, C., & Adeniyi, A. (2021). Verification of pore size effect on aqueous-phase adsorption kinetics: A case study of methylene blue. *Colloids and Surfaces A: Physicochemical and Engineering Aspects*, *626*. https://doi.org/10.1016/j.colsurfa.2021.127119

Jensen, K., Christensen, M., Juhas, P., Tyrsted, C., Bøjesen, E., Lock, N., Billinge, S., & Iversen, B. (2012). Revealing the mechanisms behind sno2 nanoparticle formation and growth during hydrothermal synthesis: An in situ total scattering study. *Journal of the American Chemical Society*, *134*(15), 6785–6792. https://doi.org/10.1021/ja300978f

Jorgetto, A. d. O., Boldrin Zanoni, M., & Orlandi, M. (2023). Assessment of the superior photocatalytic properties of sn2+-containing sno2 microrods on the photodegradation of methyl orange. *Scientific Reports*, *13*(1), 14774. https://doi.org/10.1038/s41598-023-40659-8

Karmaoui, M., Jorge, A., McMillan, P., Aliev, A., Pullar, R., Labrincha, J., & Tobaldi, D. (2018). One-step synthesis, structure, and band gap properties of sno2 nanoparticles made by a low temperature nonaqueous sol-gel technique. *ACS Omega*, *3*(10), 13227–13238. https://doi.org/10.1021/acsomega.8b02122

Kerrami, Z., Sibari, A., Mounkachi, O., Benyoussef, A., & Benaissa, M. (2020). Improved photoelectrochemical properties of strained sno2. *International Journal of Hydrogen Energy*, *45*(19), 11035–11039. https://doi.org/10.1016/j.ijhydene.2018.03.199

Khader, E., Muslim, S., Saady, N., Ali, N., Salih, I., Mohammed, T., Albayati, T., & Zendehboudi, S. (2024). Recent advances in photocatalytic advanced oxidation processes for organic compound degradation: A review. *Desalination and Water Treatment*, *318*, 100384. https://doi.org/10.1016/j.dwt.2024.100384

Khan, S., Noor, T., Iqbal, N., & Yaqoob, L. (2024). Photocatalytic dye degradation from textile wastewater: A review. *ACS Omega*, *9*(20), 21751–21767. https://doi.org/10.1021/acsomega.4c00887

Kim, S., Choi, M., & Choi, H. (2016). Photocatalytic activity of sno2 nanoparticles in methylene blue degradation. *Materials Research Bulletin*, *74*, 85–89. https://doi.org/10.1016/j.materresbull.2015.10.024

Klein, J., Kampermann, L., Mockenhaupt, B., Behrens, M., Strunk, J., & Bacher, G. (2023). Limitations of the tauc plot method. *Advanced Functional Materials*, *33*(47). https://doi.org/10.1002/adfm.202304523

Lalasari, L., Arini, T., Andriyah, L., Firdiyono, F., & Yuwono, A. (2018). Electrical, optical and structural properties of fto thin films fabricated by spray ultrasonic nebulizer technique from sncl4 precursor. *PROCEEDINGS OF THE INTERNATIONAL SEMINAR ON METALLURGY AND MATERIALS*, 020001. https://doi.org/10.1063/1.5038283

Li, Y., Guo, Y., Tan, R., Cui, P., Li, Y., & Song, W. (2009). Synthesis of sno2 nano-sheets by a template-free hydrothermal method. *Materials Letters*, *63*(24-25), 2085–2088. https://doi.org/10.1016/j.matlet.2009.06.060

Lin, J., Ye, W., Xie, M., Seo, D., Luo, J., Wan, Y., & Van der Bruggen, B. (2023). Environmental impacts and remediation of dye-containing wastewater. *Nature Reviews Earth & Environment*, *4*(11), 785–803. https://doi.org/10.1038/s43017-023-00489-8

Luque, P., Nava, O., Soto-Robles, C., Chinchillas-Chinchillas, M., Garrafa-Galvez, H., Baez-Lopez, Y., Valdez-Núñez, K., Vilchis-Nestor, A., & Castro-Beltrán, A. (2020). Improved photocatalytic efficiency of sno2 nanoparticles through green synthesis. *Optik*, *206*, 164299. https://doi.org/10.1016/j.ijleo.2020.164299

Makuła, P., Pacia, M., & Macyk, W. (2018). How to correctly determine the band gap energy of modified semiconductor photocatalysts based on uv–vis spectra. *The Journal of Physical Chemistry Letters*, *9*(23), 6814–6817. https://doi.org/10.1021/acs.jpclett.8b02892

Mamakhel, A., Søndergaard, M., Borup, K., & Brummerstedt Iversen, B. (2020). Continuous flow hydrothermal synthesis of rutile sno2 nanoparticles: Exploration of ph and temperature effects. *Journal of Supercritical Fluids*, *166*. https://doi.org/10.1016/j.supflu.2020.105029

Mishra, S., & Ahmaruzzaman, M. (2022). Tin oxide based nanostructured materials: Synthesis and potential applications. *Nanoscale*, *14*(5), 1566–1605. https://doi.org/10.1039/d1nr07040a

Mohamadpour, F., & Amani, A. (2024). Photocatalytic systems: Reactions, mechanism, and applications. *RSC Advances*, *14*(29), 20609–20645. https://doi.org/10.1039/D4RA03259D

Pandey, P., Kurchania, R., & Haque, F. (2015). Controlled hydrothermal synthesis, structural and optical analysis of nanometer-sized zno spheres. *Optik*, *126*(2), 301–303. https://doi.org/10.1016/j.ijleo.2014.08.160

Sagadevan, S., Lett, J., Alshahateet, S., Fatimah, I., Weldegebrieal, G., Le, M., Leonard, E., Paiman, S., & Soga, T. (2022). Photocatalytic degradation of methylene blue dye under direct sunlight irradiation using sno2 nanoparticles. *Inorganic Chemistry Communications*, *141*. https://doi.org/10.1016/j.inoche.2022.109547

Sato, K., Yokoyama, Y., Valmalette, J.-C., Kuruma, K., Abe, H., & Takarada, T. (2013). Hydrothermal growth of tailored sno2 nanocrystals. *Crystal Growth & Design*, *13*(4), 1685–1693. https://doi.org/10.1021/cg400013q

Schwartz, M., Rajah, S., Askury, A., Putthapiban, P., & Djaswadi, S. (1995). The southeast asian tin belt. *Earth-Science Reviews*, *38*, 95–293. https://doi.org/10.1016/0012-8252(95)00004-T

Septiningrum, F., Yuwono, A., Maulana, F., Nurhidayah, E., Dhaneswara, D., Sofyan, N., Hermansyah, H., & Purwanto, W. (2024). Mangosteen pericarp extract mediated synthesis of ag/tio2 nanocomposite and its application on organic pollutant degradation by adsorption-photocatalytic activity. *Current Research in Green and Sustainable Chemistry*, *8*. https://doi.org/10.1016/j.crgsc.2023.100394

Shabna, S., Dhas, S., & Biju, C. (2023). Potential progress in sno2 nanostructures for enhancing photocatalytic degradation of organic pollutants. *Catalysis Communications*, *177*, 106642. https://doi.org/10.1016/j.catcom.2023.106642

Skripkin, E., Podurets, A., Kolokolov, D., Burmistrova, A., Bobrysheva, N., Osmolowsky, M., Voznesenskiy, M., & Osmolovskaya, O. (2024). Ultrasmall sno2 nanoparticles: Influence of o-vacancies on the photocatalytic degradation of dyes. *ACS Applied Nano Materials*, *7*(6), 6093–6108. https://doi.org/10.1021/acsanm.3c05997

Sukriti & Chand, P. (2019). Effect of ph values on the structural, optical and electrical properties of sno2 nanostructures. *Optik*, *181*, 768–778. https://doi.org/10.1016/j.ijleo.2018.10.203

Sun, C., Yang, J., Xu, M., Cui, Y., Ren, W., Zhang, J., Zhao, H., & Liang, B. (2022). Recent intensification strategies of sno2-based photocatalysts: A review. *Chemical Engineering Journal*, *427*, 131564. https://doi.org/10.1016/j.cej.2021.131564

Suryanarayana, C., & Norton, M. (1998). *X-ray diffraction*. Springer US. https://doi.org/10.1007/978-1-4899-0148-4

Talebian, N., & Jafarinezhad, F. (2013). Morphology-controlled synthesis of sno2 nanostructures using hydrothermal method and their photocatalytic applications. *Ceramics International*, *39*(7), 8311–8317. https://doi.org/10.1016/j.ceramint.2013.03.101

Thommes, M., Kaneko, K., Neimark, A., Olivier, J., Rodriguez-Reinoso, F., Rouquerol, J., & Sing, K. (2015). Physisorption of gases, with special reference to the evaluation of surface area and pore size distribution (iupac technical report). *Pure and Applied Chemistry*, *87*(9-10), 1051–1069. https://doi.org/10.1515/pac-2014-1117

Van Pham, V., Mai, D., Bui, D., Van Man, T., Zhu, B., Zhang, L., Sangkaworn, J., Tantirungrotechai, J., Reutrakul, V., & Cao, T. (2021). Emerging 2d/0d g-c3n4/sno2 s-scheme photocatalyst: New generation architectural structure of heterojunctions toward visible-light-driven no degradation. *Environmental Pollution*, *286*, 117510. https://doi.org/10.1016/j.envpol.2021.117510

Wan, W., Li, Y., Ren, X., Zhao, Y., Gao, F., & Zhao, H. (2018). 2d sno2 nanosheets: Synthesis, characterization, structures, and excellent sensing performance to ethylene glycol. *Nanomaterials*, *8*(2), 112. https://doi.org/10.3390/nano8020112

Wu, N., Shi, E., Zheng, Y., & Li, W. (2002). Effect of ph of medium on hydrothermal synthesis of nanocrystalline cerium(iv) oxide powders. *Journal of the American Ceramic Society*, *85*(10), 2462–2468. https://doi.org/10.1111/j.1151-2916.2002.tb00481.x

Yu, S., Zhang, C., & Yang, H. (2023). Two-dimensional metal nanostructures: From theoretical understanding to experiment. *Chemical Reviews*, *123*(7), 3443–3492. https://doi.org/10.1021/acs.chemrev.2c00469

Yuwono, A., Septiningrum, F., Nagaria, H., Sofyan, N., Dhaneswara, D., Arini, T., Andriyah, L., Lalasari, L., Ardianto, Y., & Pawan, R. (2023). The hydrothermal synthesis of sno2 nanoparticles derived from tin chloride precursor for the electron transport layer of perovskite solar cells. *EUREKA: Physics and Engineering*, (4), 189–198. https://doi.org/10.21303/2461-4262.2023.002947

Zhang, X., Zhu, H., Xu, M., Cao, S., Hu, R., Peng, L., Zhang, C., & Zhang, D. (2025). Ph-mediated hydrothermal synthesis of sno2 for enhanced ethanol sensing: Structural regulation and performance optimization. *Journal of Alloys and Compounds*, *1025*. https://doi.org/10.1016/j.jallcom.2025.180334

Zhu, J., Tay, B., & Ma, J. (2007). Hydrothermal synthesis and characterization of mesoporous sno2/sno2–sio2 on neutral template. *Journal of Materials Processing Technology*, *192-193*, 561–566. https://doi.org/10.1016/j.jmatprotec.2007.04.071